Self-Assembly of Magnetic Nanoparticles in Evaporating Solution

JiYeon Ku,[†] Deborah M. Aruguete,[†,§] A. Paul Alivisatos,[†,‡] and Phillip L. Geissler*[,†,¶]

[†]Department of Chemistry, University of California, Berkeley, California 94720, United States
[‡]Materials Sciences Division and [¶]Chemical Sciences Division, Lawrence Berkeley National Laboratory, Berkeley, California 94720, United States

S *Supporting Information*

ABSTRACT: When deposited from an evaporating solution onto a substrate, even nondescript nanoparticles can organize into intricate spatial patterns. Here we show that a simple but long-ranged anisotropy in nanoparticles' interactions can greatly enrich this scenario. In experiments with colloidal Co nanocrystals, which bear a substantial magnetic dipole, we observe assemblies quite distinct from those formed by nonmagnetic particles. Reflecting the strongly none-quilibrium nature of this process, nanocrystal aggregates also differ substantially from expected low-energy arrangements. Using coarse-grained computer simulations of dipolar nanoparticles, we have identified several dynamical mechanisms from which such unusual morphologies can arise. For particles with modest dipole moments, transient connections between growing domains frustrate phase separation into sparse and dense regions on the substrate. Characteristic length scales of the resulting cellular networks depend non-monotonically on the depth of quenches we use to mimic the effects of solvent evaporation. For particles with strong dipole moments, chain-like aggregates formed at early times serve as the agents of assembly at larger scales. Their effective interactions drive the formation of layered loop structures similar to those observed in experiments.
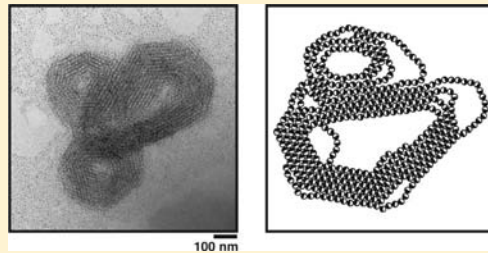
INTRODUCTION

Nanocrystals possess a wide range of unique properties with great potential in optical, electronic, biomedical, and computing applications.[1-7] Magnetic nanocrystals in particular are promising building blocks for high-performance nanodevices for applications such as information storage and recording media.[8-11] Achieving this enormous promise, however, requires controlled fabrication of specific structures using nanoparticles as elementary units. Due to the small size of these particles, conventional means of positioning nanometer-scale objects are quite limited. Therefore, identifying effective and dependable means of pattern formation through spontaneous organization would be a key step toward linking their potential as new materials to practical applications.[12-15]

From a thermodynamic perspective, achieving control over nanoparticles' arrangements would seem to be a conceptually straightforward matter of tuning their interactions so that desired structures lie lower in free energy than alternative arrangements. Several experimental and computational studies have taken such an approach, attempting to expose relationships between particles' anisotropies and their aggregate morphologies at equilibrium.[16-25] Their results demonstrate rich possibilities, whose realizations in many cases must await advances in synthetic capabilities. More problematic than the difficulty of making such nanoparticles, however, is the possibility that some of these equilibrium states are nearly inaccessible from an initially dispersed state, due to extreme dynamic bottlenecks and deep kinetic traps. Indeed, results of several studies suggest that a competition between kinetics and thermodynamics shapes self-assembly quite generally at this length scale.[23,26-31]

A common method for initiating the aggregation of nanocrystals is to evaporate the solvent in which they were made.[32-41]

This process typically involves two distinct kinds of phase changes. One is clearly the conversion of solvent from liquid to vapor, which is accompanied by strong density fluctuations at the nanoscale. The other is a condensation of nanocrystal solutes, more precisely a segregation of solute-rich and solute-poor regions. This latter transition can be driven both by concentration of nanocrystals through solvent attrition and by an effective increase in solute−solute interaction strength through reduced solvent screening.[41,42] The accompanying aggregation on the way toward macroscopic segregation is extremely slow, with characteristic length scales growing sublinearly in time.[43] Together with strong attenuation of nanocrystal mobility in the absence of solvent, this slow growth ensures the importance of kinetic factors in determining structures that form on laboratory time scales.

Through mechanisms of coarsening and its coupling to solvent density fluctuations, even particles that lack complex interactions can achieve long-lived spatial arrangements through drying that are intricate and varied.[39−41,44−47] These structures could be viewed as metastable intermediates that impede progress to ordered equilibrium states. Alternatively, they could be considered as effective end-products of assembly whose relationship with interparticle interactions is subtle and intimately tied to the dynamic protocols that produce them. Taking this latter view, we have explored how basic mechanisms of drying-mediated assembly are modified by particle interactions that are both anisotropic and long-ranged. Our experiments, described in the following section, focus on aggregation of ε-Co nanocrystals,[48,49] which bear substantial magnetic moments.

Following solvent evaporation, we observe mesoscale structures that differ qualitatively from those previously reported for more isotropic, nonmagnetic particles. Numerical simulations of a coarse-grained model generate similar morphologies under nonequilibrium conditions designed to mimic the dynamics of evaporating solutions. Computed trajectories point toward distinct modes of pattern formation shaped by an interplay among van der Waals and dipolar forces, dynamic modulation of effective solute interaction strengths, and transient spatial heterogeneities. These various regimes of assembly are discussed in the Results and Discussion section.

■ EXPERIMENTAL METHODS AND RESULTS

Synthesis of Cobalt Nanocrystals. All synthesis and processing of the cobalt nanocrystals were performed under air-free and water-free conditions. Cobalt nanocrystals were synthesized via previously established methods[25] that will be briefly described here. To summarize, dicobaltoctacarbonyl (dissolved in 1,2-dichlorobenzene, or DCB) was rapidly injected into a boiling solution of oleic acid and trioctylphosphine oxide (TOPO) in DCB. Aliquots (in nitrogen-purged vials) were collected 1, 2, 3, and 5 min after injection and immediately transferred into an argon drybox. X-ray diffraction confirmed that the samples were ε-cobalt, a phase of cobalt that has only been found in nanocrystals.[48] ε-Co is isostructural with a high-temperature phase of manganese (β-Mn) and is a cubic, non-close-packed structure. Three separate batches of nanocrystals were used to make nanocrystal assemblies, with diameters of 10.8 $\pm$1.9, 11.2 $\pm$ 1.2, and 10.0 $\pm$ 2.5 nm.

Preparation and Analysis of Nanocrystal Assemblies. All transmission electron microscopy (TEM) samples were prepared and stored under air-free and water-free conditions. Samples were made by dipping 400-mesh copper carbon-coated grids into concentrated solutions of nanoparticles in DCB (as obtained from the syntheses). Note that, as no cleaning of the synthesis products was performed, it was likely that the nanocrystal solution contained some free oleic acid and TOPO. Excess liquid was wicked away with a Kimwipe, and grids were allowed to dry for a minimum time of 2 h. All TEM measurements were performed on an FEI Tecnai 20 microscope with a 200 kV accelerating voltage.

Evaporation of nanocrystal solutions caused the nanocrystals to self-assemble into various ordered structures, as shown in Figures 1 and 5. These assemblies mostly comprise a few particle monolayers, distinct but superposed, in each of which particles are hexagonally packed in close proximity. In contrast to the single-file chains and loops observed in previous studies of magnetic nanocrystal assembly, our experiments produce stripes and angular loops that are many particles wide. As shown in Figure 1b, the edges of assembled superstructures are rough on the nanometer scale of individual particles. Their heights typically decrease to 1−2 monolayers within ∼100 nm of their horizontal boundaries. Structured monolayers partially overlaying other, distinctly patterned monolayers (as in Figures 5 and SI 1 (Supporting Information)) were also observed. The diversity of observed structures, all produced by the same experimental protocol, suggests that evaporation created solution conditions which vary strongly on the micrometer scale during deposition.

The shape or faceting of nanocrystals has been shown to play a role in ordered self-assembly,[9,50,51] resulting in nanocrystal assemblies with preferred crystallographic orientations. Also, in the case of magnetic nanocrystal assembly, preferred crystallographic orientations might be expected, due to magnetocrystalline anisotropy, or the alignment of magnetic dipoles in a crystal along a given axis. To determine if these factors could be influencing assembly, selected area electron diffraction (SAED) was used to examine various loops and ribbon formations. No clear preferred orientations were found, suggesting that faceting was not strongly affecting self-assembly and that magnetocrystalline anisotropy stabilization energy was not significant enough to affect the crystallographic orientation of the nanocrystals on the time scale of deposition.
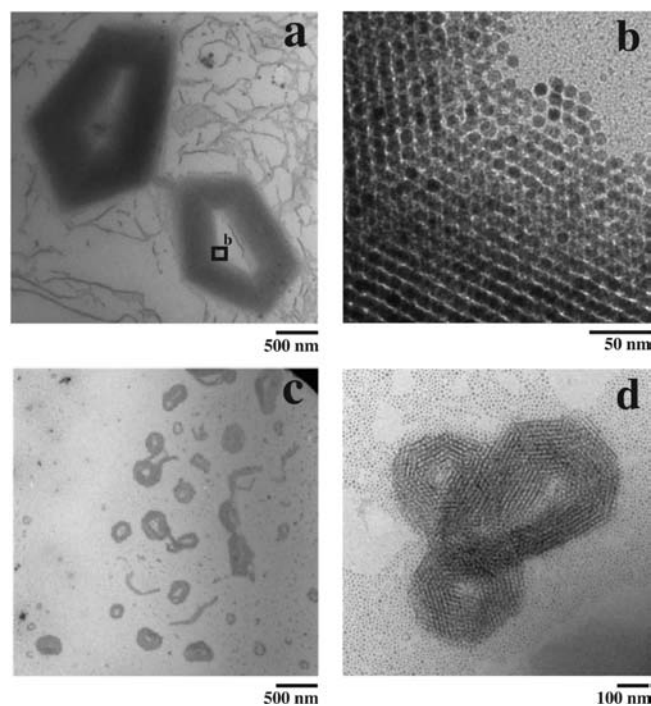

Figure 1. TEM images of evaporation-driven self-assembly of ε-Co nanocrystals. Hollow, irregular polygons spanning several micrometers (a) and smaller angular loop structures (c,d) are among many unique patterns observed in experiment. (b) A magnification of the inner edge of the lower right polygon in (a).

■ MONTE CARLO SIMULATIONS

Model. The time and length scales involved in this example of nanoparticle self-assembly far exceed those accessible to atomistically detailed computer simulations. We construct a coarse-grained model (Figure 2a) that resolves only a few key features of interparticle forces. For each pair of particles i and j, we adopt a potential energy $u_{ij} = u_{ij}^{(\text{hard}-\text{core})} + u_{ij}^{(\text{dispersion})} + u_{ij}^{(\text{dipole})}$, whose general form follows from models that have been widely applied in the context of dipolar colloids.[52−54] Specifically, we consider magnetic nanocrystals as volume-excluding spheres, bearing point dipoles at their centers, which additionally attract one another isotropically at short range through a van der Waals-like contribution. In its explicit components, this caricature neglects almost entirely nanocrystals' internal structure, e.g., local variations of dipole density within the crystalline lattice and the sizable layer of organic ligands passivating each particle's surface. It further neglects the role of solvent in screening short-ranged attractions. In this section we address these concerns while detailing the mathematical form of the model potential energy function.

Though vastly smaller than its macroscopic counterpart, a typical nanocrystal still comprises hundred of thousands of atoms. At the distance of closest approach permitted by passivating ligands (∼1 nm), the magnetic core of a Co nanocrystal should thus appear as a nearly uniform sphere of dipole density. In this approximation, the magnetic field it generates is identical to that of a point dipole situated at its center. We have verified this argument by comparing the interactions between two nanocrystals, represented as close-packed collections of dipolar atoms (Figure 2b), with those of corresponding point dipoles. Figure 2c,d shows that the resulting
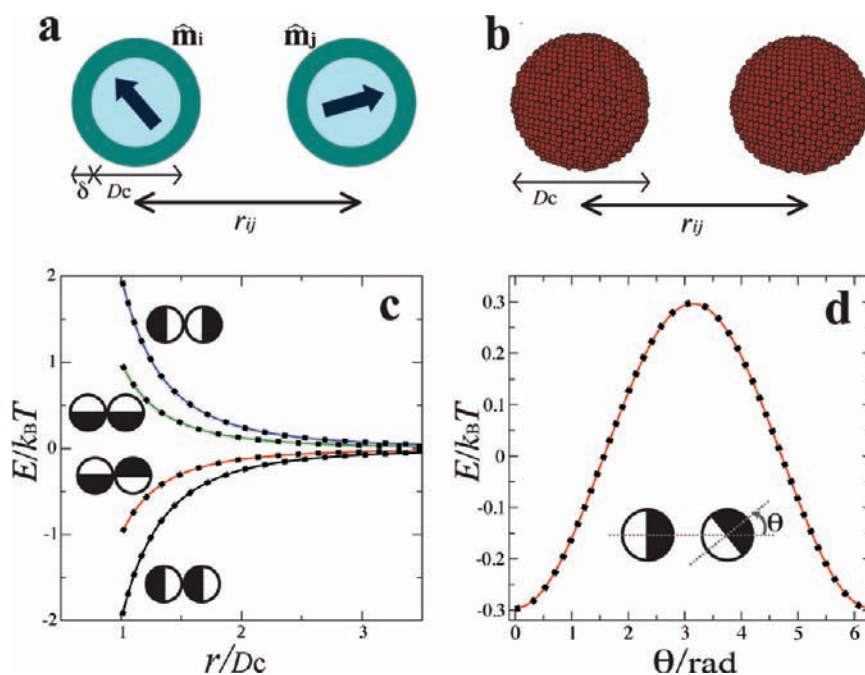
Figure 2. (a) Model of magnetic nanoparticles as spheres with a ferromagnetic core diameter of D_c and a surfactant layer of thickness δ. Each particle also has a point dipole $\hat{\mathbf{m}}$ embedded at the center. (b) Spherical clusters of dipolar particles, whose magnetic interaction energies we compare with those of the point dipoles in (a). A large collection of particles were first arranged in a hexagonal close-packed lattice; clusters were then constructed by eliminating all particles outside a sphere of diameter D_c. Spheres with 53, 748, and 20 041 particles were used for the energy calculation. Individual dipole moments within a cluster point in the same direction, and the magnitude is normalized such that the total dipole moment of a cluster equals that of one point dipole. (c) Magnetic interaction energies of two nanoparticles, plotted as a function of separation distance r, for point dipoles (solid lines) and for clusters (dotted lines). Results are shown for four different orientations, as indicated by half-filled circles. (d) Magnetic interaction energies of two nanoparticles separated by a distance $r_{ij} = 1.5D_c$, plotted as a function of relative orientation θ. Here and in subsequent figures, half-filled circles represent nanoparticles whose dipole moments point from the filled half to the unfilled half.

energies are essentially indistinguishable, regardless of the particles' orientations. The simple potential energy,

$$\beta u_{ij}^{(\text{dipole})} = \frac{\lambda}{r_{ij}^3} \hat{\mathbf{m}}_i \cdot [\mathbf{I} - 3\hat{\mathbf{r}}_{ij}\hat{\mathbf{r}}_{ij}] \cdot \hat{\mathbf{m}}_j \qquad (1)$$

should thus accurately represent magnetic interactions between two particles i and j, whose dipoles are oriented along the unit vectors $\hat{\mathbf{m}}_i$ and $\hat{\mathbf{m}}_j$, respectively. The unit vector $\hat{\mathbf{r}}_{ij}$ points from i to j, and $\mathbf{I}$ denotes the unit tensor. We express all distances in units of D_c, the diameter of a particle's magnetic core; e.g., r_{ij} is the distance between the centers of particles i and j relative to D_c. We further adopt $k_B T = \beta^{-1}$ as a unit of energy, yielding $\lambda = m^2/(4\pi\mu_0 D_c^3 k_B T)$ as a dimensionless measure of dipole−dipole interaction strength; here, m is the magnitude of a particle's net magnetic dipole moment, and μ_0 is the magnetic constant. Long-range contributions to magnetostatic energies were computed using Ewald sums[55] with conducting boundary conditions in all simulations with periodic boundaries.

Several studies have focused separately on dispersion forces between two nanocrystal cores and on those between their passivating ligands.[42,56−58] For the particles we have studied in experiments, neither of these contributions should be especially large in solution, relative to the energy scale of typical thermal excitations. Highly polarizable crystalline cores cannot approach closely due to the ligand layers, and the solvent environment thoroughly screens interactions between mildly polarizable organic ligands. In air, however, ligand−ligand attractions can be quite substantial, many times larger than $k_B T$ for particles near contact.[58,59] The evaporation of solvent thus has the effect of

"turning on" strong and short-ranged attractions, as emphasized in ref 58. We take the functional form of the dispersion potential for a pair of particles i and j from ref 60:

$$\beta u_{ij}^{(\text{dispersion})} = -(2.025)A[(r_{ij}^2 - 1)^{-1} + r_{ij}^{-2} + 2\ln(1 - r_{ij}^{-2})] \qquad (2)$$

Although this specific form was devised to mimic van der Waals attractions between two crystalline cores, we use it primarily to represent solvent-mediated interactions between ligand shells. For our purposes, eq 2 simply describes an isotropic attraction that operates only when two particles are near contact. Our simulation results do not change qualitatively when it is replaced by a different potential of limited range, specifically a Lennard-Jones potential.

The numeric scaling factor on the right-hand side of eq 2 has been chosen so that $\beta u_{ij}^{(\text{dispersion})} \simeq -A$ when two particles contact one another, i.e., when their separation distance exceeds D_c by an amount representing volume exclusion among the intervening ligands. Estimating the thickness of a particle's ligand layer as $\delta = 0.1D_c$, we define contact precisely as $r_{ij} = 1 + 2\delta$. In refs 52 and 53, volume exclusion was enforced by a smooth but sharply repulsive potential. For simplicity we use instead a hard-sphere potential,

$$u_{ij}^{(\text{hard-core})} = \begin{cases} \infty, & r_{ij} \leq 1 + 2\delta \\ 0, & r_{ij} > 1 + 2\delta \end{cases} \qquad (3)$$

appropriate for very densely packed ligand shells.

Simulation Methods. The principal objective of our simulations is to identify and characterize features of drying-mediated

assembly that emerge when particle interactions favor structured aggregates over simply compact domains. The results of ref 41 for self-assembly via short-ranged isotropic interactions thus serve as important points for comparison. Following that work, we propagate dynamics of a collection of substrate-bound nanoparticles via a kinetic Monte Carlo (MC) scheme with the conventional Metropolis acceptance criterion for a closed system in contact with a heat bath.[61,62]

Our quasi-two-dimensional simulations feature particles, as well as their magnetic moments, confined to a plane parallel to the substrate. In exploratory calculations that permitted dipoles to rotate into the third dimension, the favorable energies of head-to-tail alignment greatly limited out-of-plane fluctuations for the values of λ we study. The focus on aggregation within a microscopic distance from the substrate is motivated by our experimental results, which indicate perpendicular growth of at most a few particle diameters. In other contexts, the underlying conjecture that drying-mediated assembly occurs chiefly within a thin film of solvent has been supported by experiments[40,46] as well as simulations.[63]

We include as individual MC trial moves both translation and rotation of a randomly selected nanoparticle. Unlike the lattice model of ref 41, our calculations allow particles to move continuously in two-dimensional space. In particular, displacements in Cartesian coordinates and dipole angle were drawn from Gaussian distributions with zero mean and variances that yield acceptance rates of roughly 50%. This generalization from the lattice dynamics of ref 41 is essential to capture orientationally distinct patterning due to the interplay between packing and the energetics of dipole alignment. Small ring-like structures, for example, are common to dipolar systems but awkward to represent on a square lattice.

As initial conditions for some assembly trajectories, we sampled configurations Γ_N (specifying both the positions and orientations of N indistinguishable particles) from grand canonical distributions,

$$P(\Gamma) = \Xi^{-1}\left(\frac{\rho_0}{2\pi}\right)^N \exp[\mu^* N - \beta U(\Gamma_N)] \qquad (4)$$

where U is the energy and Ξ is the grand canonical partition function. The dimensionless quantity μ^* expresses chemical potential relative to that of an ideal gas at density $\rho_0 = D_c^{-2}$, scaled by $k_B T$. Acceptance probabilities for the corresponding grand canonical Monte Carlo (GCMC) simulations are[61]

$$\mathrm{acc}(\Gamma_N \longrightarrow \Gamma'_{N+1}) = \min\left[1, \frac{\rho_0 L^2}{N+1}\exp(\mu^* - \beta[U(\Gamma'_{N+1}) - U(\Gamma_N)])\right] \qquad (5)$$

when a particle is introduced at a random location and with random orientation, and

$$\mathrm{acc}(\Gamma_N \longrightarrow \Gamma''_{N-1}) = \min\left[1, \frac{N}{\rho_0 L^2}\exp(-\mu^* - \beta[U(\Gamma''_{N-1}) - U(\Gamma_N)])\right] \qquad (6)$$

when a randomly selected particle is deleted. L is the side length of the square simulation box.

One could mimic the intraparticle dynamics associated with superparamagnetism of Co nanocrystals[64] in MC simulations by attempting dipole inversion at an appropriate rate. The simulations described in this paper do not include such trial moves. As with dipole rotations into the third dimension, test calculations

suggest that fluctuations of this nature are strongly suppressed once particles begin to associate.

The process of evaporation was described explicitly in ref 41 through fluctuations of a lattice gas, drawing attention to the influence of microscopic variations in solvent density. As a first step, the work described in this paper adopts more primitive descriptions of drying dynamics. In some cases we progressively increase the value of A over time, representing the effective strengthening of van der Waals attractions as solvent screening attenuates. In other cases we mimic spatial heterogeneities associated with nucleation and growth of vapor bubbles by selectively adding particles to localized regions of the substrate. Details of these procedures along with their results are described in the following section.

■ RESULTS AND DISCUSSION

The deposited structures we have generated in experiments represent systems very far from equilibrium. As such, the fates of assembly cannot be specified by a handful of macroscopic parameters (e.g., temperature and concentration) and material properties (e.g., interactions among nanoparticles, solvent, and substrate). The central importance of history requires in simulations not only that we sample ensembles of long trajectories, but also that we consider explicitly how environmental conditions change over time.

We have examined three distinct evaporation scenarios, corresponding to different relative time scales associated with processes of deposition, aggregation, and desolvation.

- Adiabatic drying
- Spatially homogeneous drying
- Spatially heterogeneous drying

In the first scenario, deposition and aggregation of nanoparticles on the substrate occur adiabatically (i.e., the collection of substrate-bound particles remains in local equilibrium), followed by instantaneous disappearance of solvent from the particles' immediate surroundings. The second scenario considers a more gradual, though far from reversible, process of desolvation. The third scenario is distinguished by spatially nonuniform deposition of material onto the substrate, which fosters irreversible aggregation and, in the case of strong dipoles, generates a unique class of patterning mechanisms. This survey of conditions for assembly dynamics is by no means exhaustive, especially if fine details of the evaporation protocol are considered as control parameters. But it does represent diverse kinetic and structural possibilities, including several extreme limits, and sheds light on pathways leading to many of the unusual morphologies we have observed in experiments.

Adiabatic Drying. The initial stages of evaporation principally effect an enhancement of nanoparticles' concentration in solution and a consequent increase in substrate coverage. In this section we imagine that concomitant relaxation and diffusion of substrate-bound aggregates are facile on the time scale of deposition. The final steps of evaporation influence assembly in rather different ways, by modifying effective interaction strengths and ultimately immobilizing particles on the substrate. For the first assembly scenario, we consider these later processes to occur so rapidly that material on the substrate cannot respond to altered thermodynamic driving forces. Instead, configurations determined by dynamics at earlier times become instantaneously and inexorably fixed.

With this set of assumptions, final assembled structures represent equilibrium states of systems comprising nanoparticles
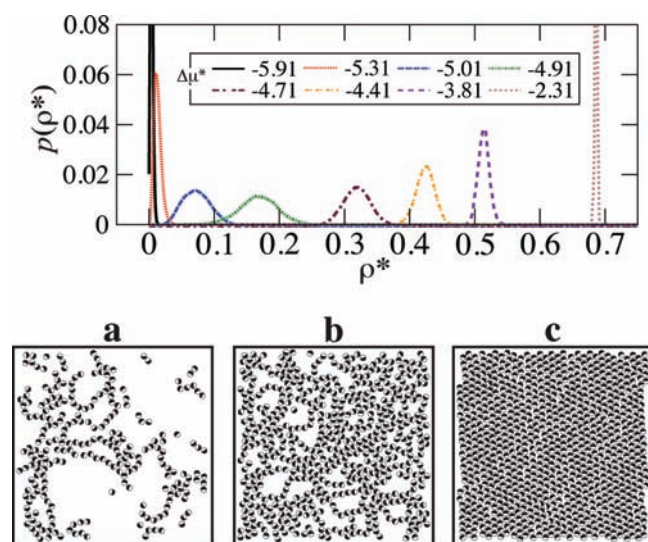
Figure 3. Probability distributions $p(\rho^*)$ of reduced density $\rho^* = ND_c^2/L^2$, where N is the total number of particles and L^2 is the area of the simulation box ($L = 35D_c$). All results shown were obtained from grand canonical Monte Carlo simulations at $\lambda = 6.0$, $A = 1.0$. Curves correspond to $\mu^* = -5.91, -5.31, -5.01, -4.91, -4.71, -4.41, -3.81,$ and -2.31 (from left to right). Snapshots of typical configurations at $\mu^* = -4.88$ (a), -4.11 (b), and -2.31 (c) are also shown.

that are adjacent to the substrate but otherwise completely surrounded by solvent. They are *not* typical of fully dried systems at equilibrium, which would be overwhelmingly biased by van der Waals attractions among passivating ligands. Based on continuum calculations and simulations of similar nanoparticles,[58,59] the favorable free energy of interaction between two neighboring ligand shells in air should be orders of magnitude larger than k_BT, i.e., $A \approx 100-1000$.

Exploiting the connection with appropriate equilibrium states, we have sampled the products of self-assembly using the GCMC methods previously described in the Model and Simulation Methods sections. Example configurations and probability distributions are shown in Figure 3 for several values of chemical potential μ^*.

As in previous studies of dipolar particles in two and three dimensions,[65−70] equilibrium structures can be classified into a few basic types. At very low μ^*, well-separated clusters clearly manifest the archetypal head-to-tail organization stabilized by dipolar interactions. As μ^* increases, these chain-like clusters first grow and interact with one another (as in Figure 3a) and then coalesce to form percolating networks (as in Figure 3b). Typical configurations of nanocrystal aggregates at high μ^* are nearly close-packed and possess a large net magnetization, with dipoles aligned along one of the triangular lattice vectors (as in Figure 3c).

For the system sizes we have studied, i.e., square boxes with side length $L = 35D_c$, the number of particles N can vary noticeably at a given thermodynamic state. Figure 3 shows normalized histograms of number density $\rho = N/L^2$ for several values of μ^* spanning the range of structures described above. To the extent that a low-μ^* state can be considered as an ideal gas of clusters with size $N_{cluster}$, density fluctuations in dilute states are limited in breadth, $\langle \delta\rho^2 \rangle = N_{cluster}\langle\rho\rangle/L^2$. Densely packed systems also have well-defined densities, as reflected by very low compressibility, $\kappa = \rho^{-1}(\partial\rho/\partial p)_T = \beta(L/\rho)^2\langle\delta\rho^2\rangle$. By contrast, intermediate values of μ^* yield very compressible networks with

corresponding large density fluctuations. As one consequence, the products of assembly resulting from a unique drying protocol can be diverse on this length scale, even in the regime of adiabatic aggregation.

We do not expect the extreme relationships among time scales that defines this drying scenario to be particularly realistic. Instead, we view the results shown in Figure 3 as points of reference for understanding self-assembly under more complex circumstances. These locally equilibrated states further serve as intermediates in other drying scenarios featuring more gradual desolvation. In that context, which we discuss in the next section, the significance of large density fluctuations lies in the possibility of enriching the diversity of assembly pathways associated with a single set of external conditions.

Spatially Homogeneous Drying. Because the length and time scales characteristic of nanoparticle motion are commensurate with those of the solvent density fluctuations that advance drying, it is likely more appropriate to consider a desolvation process that is accompanied by some degree of solute reorganization. Reference 41 suggests models and methods for treating these dynamics on similarly explicit footings. Here, in a first exploration of the role of anisotropic forces in evaporation-driven self-assembly, we instead describe the disappearance of solvent in schematic ways informed by the results of that work.

In this section we mimic gradual desolvation by following the dynamics of nanoparticles in a continuous and spatially uniform solvent whose density decreases in stages. More specifically, this mean-field approach varies, over time, the effective strength of short-range attractions. We begin with a value A representative of bulk solution, step to a larger value A' signifying partial loss of solvent screening, and finally fix particles instantaneously as a caricature of immobilization following complete removal of solvent (like in the previous section).

Provided λ is not very large, association between well-solvated particles (i.e., with $A \lesssim 1$) should not overwhelm thermal excitations. If particles on the substrate have appreciable mobility in the presence of solvent, nanocrystal aggregates should thus relax readily over the course of deposition. Dipolar interactions can, in fact, facilitate this equilibration by suppressing the formation of slowly diffusing compact clusters. We therefore assume in this scenario that equilibrium is maintained until the final process of desolvation begins, i.e., until the strength of dispersion interactions is increased from A to A'. In cases where A' is itself modest, the system may remain in or close to equilibrium even after this change. When A' is significantly enhanced, however, we expect substantial nonequilibrium effects to emerge, as has been shown for aggregation of nonmagnetic nanoparticles.[27,42]

Features of these dynamics unique to dipolar particles arise most noticeably at densities for which initial configurations comprise percolating networks. At lower densities, the limited size of clusters permits rapid contraction at large A' into compact domains characteristic of non-dipolar assembly.[41,71,72] In higher-density configurations, particles are nearly close-packed even prior to desolvation, so that increasing the strength of isotropic attractions effects little structural change. We therefore adopt here a chemical potential $\mu^* = -5.45$, which for the values of A and λ we examine yields network configurations of intermediate density.

In detail, we simulate assembly trajectories by first drawing configurations from equilibrium distributions with dispersion strength A and then propagating MC dynamics at A' over a time representing the duration of the desolvation process (corresponding to 650 000 MC sweeps). Results are shown in Figures 4−6
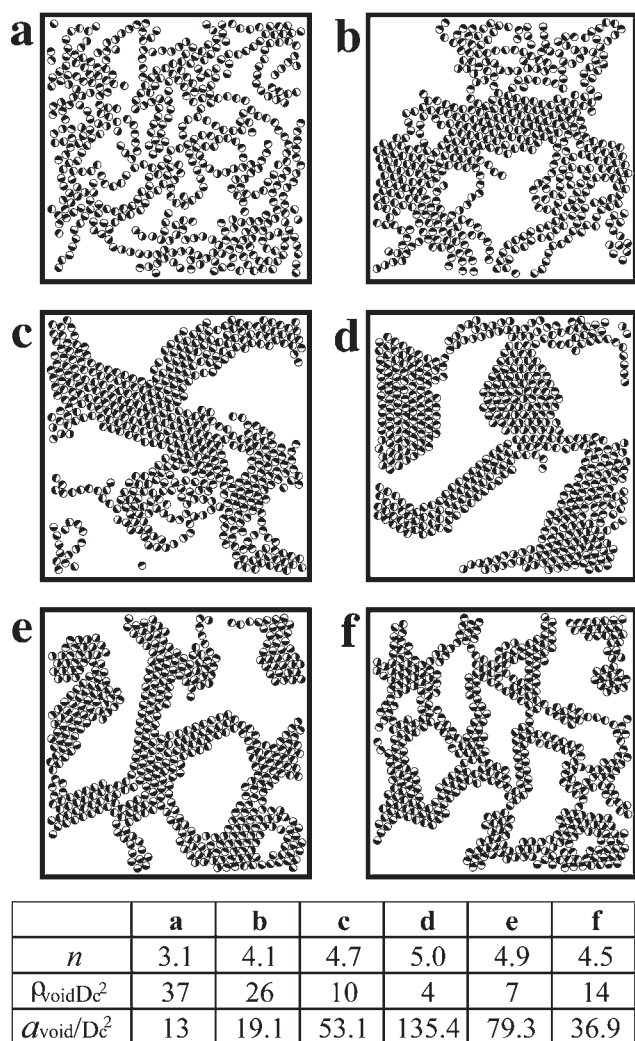
Figure 4. Representative products of spatially homogeneous drying: Initial configuration (a) taken from a GCMC calculation ($N = 482$, $\mu^* = -5.45$, $\lambda = 6.2$, $A = 1.4$) is quenched to $A' = 1.75$ (b), 2 (c), 2.25 (d), 3.00 (e), and 5 (f). In each case the box length is fixed at $L = 35D_c$. The number of nearest neighbors (n), the number density of voids ($\rho_{void}D_c^2$), and the average size of voids (a_{void}/D_c^2) for each configuration are indicated in the table.

|	**a**	**b**	**c**	**d**	**e**	**f**
n	3.1	4.1	4.7	5.0	4.9	4.5
$\rho_{void}Dc^2$	37	26	10	4	7	14
a_{void}/Dc^2	13	19.1	53.1	135.4	79.3	36.9

for $\lambda = 6.2$, $A = 1.4$, and several values of A' between 1.75 and 6. This set of parameters provides substantial contributions from dipolar forces while ensuring that relaxation preceding desolvation is indeed facile, as asserted.

Five initial conditions for these nonequilibrium trajectories were taken from GCMC sampling, providing seed configurations with $N = 439$, 453, 482, 486, and 511 particles in a periodically replicated square box of side length $35D_c$. Desolvation dynamics were evolved twice (with different random number sequences) from each configuration at each value of A', in order to gauge sensitivity both to natural variations in well-equilibrated intermediate structures and to the specific chaotic histories of individual nonequilibrium trajectories.

Example assemblies constructed in this fashion, one for each value of A' considered, are presented in Figure 4. As anticipated, the result for a modest quench $A' = 1.75$ is noticeably, however not dramatically, different from the networked configuration used to initiate each trajectory. Larger values of A' yield cellular
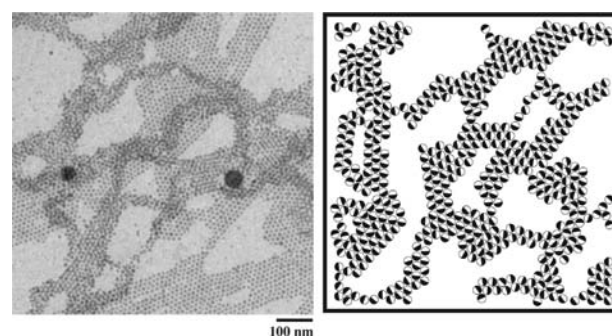
Figure 5. Experimental (left) and computational (right) results featuring network structures with empty cellular domains. The latter configuration was obtained from a quenching simulation of $N = 511$ particles identical in protocol and parameters (other than N) to that of Figure 4f. The experimental results shown on the left were obtained using the same laboratory procedures that produced the assemblies shown in Figure 1.
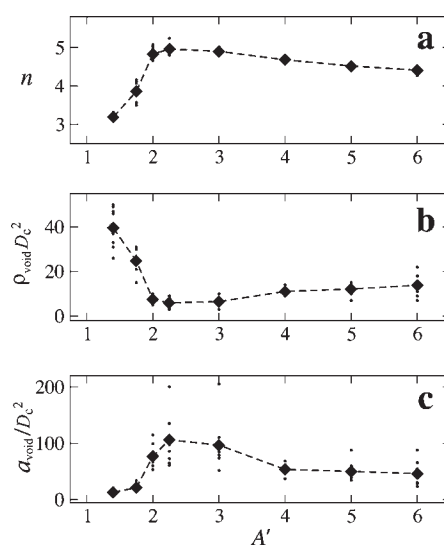
Figure 6. Statistical properties of network structures obtained from the quenching simulations illustrated by Figure 4. We consider five distinct initial configurations, all obtained from GCMC sampling as in Figure 4a. Each initial configuration was propagated in two separate quenching runs for each value of A' considered. Small points in plots of n, ρ_{void}, and a_{void} show results of individual trajectories; diamonds indicate averages over all 10 trajectories generated for each value of A'. Plots show the following properties of final, quenched configurations: (a) the average number n of particles' nearest neighbors (lying within a cutoff distance $1.5D_c$), (b) the number density ρ_{void} of voids, and (c) the size of voids (averaged over all voids in a given configuration) as functions of A'. Voids smaller in area than D_c^2 were excluded from these analyses in order to focus on mesoscale topology.

networks whose voids are much more distinct, bounded by walls that are thicker, straighter, and more orientationally ordered. We have observed comparable structures, such as the one shown in Figure 5, in experiments. These sharply faceted cellular networks bear little resemblance to representative equilibrium structures at corresponding values of λ and A'; in fact, they are atypical of any equilibrium state we have explored (scanning values of A between 1 and 5, values of λ between 5 and 8, and values of μ^* between −7 and 5).

We have quantified both the local and global character of morphologies obtained from these nonequilibrium simulations.

843

dx.doi.org/10.1021/ja107138x |*J. Am. Chem. Soc.* 2011, 133, 838–848

For the former purpose we computed average coordination numbers, which primarily reflect the thickness of cell walls. For a given particle i we define n_i as the number of other particles that lie within a cutoff distance $1.5D_c$ of i. The maximum value of n_i permitted by steric constraints is 6. Averaged over all particles in these open networks, $\langle n \rangle = N^{-1} \sum_{i=1}^{N} n_i$ typically ranges from 3 to 5.

Increasing the scale of dispersion interactions provides an ever-growing thermodynamic driving force for compaction. Indeed, equilibrium states for $\lambda = 6.2$ and $A = 1.75$ feature a single, well-packed domain (which in a periodically replicated box may or may not contact its images, depending on net density), with $\langle n \rangle \approx 6$ for the densities we consider. The fact that $\langle n \rangle$ rarely exceeds 5 in our nonequilibrium simulations evidences the potent influence of kinetics inherent to drying-mediated self-assembly.

Following the trend that would be expected from thermodynamic considerations alone, $\langle n \rangle$ increases at first for assembly simulations at successively larger values of A' (i.e., deeper quenches), as plotted in Figure 6a. At $A' \approx 2.25$, however, $\langle n \rangle$ reaches a maximum and subsequently declines with increasing A', highlighting a dominance of kinetics over thermodynamics. This non-monotonic dependence on quench depth is visually apparent in the panels of Figure 4; strips of particles that constitute cell walls clearly thicken at first with increasing A' and then attenuate. Data plotted for individual assembly trajectories in Figure 6a indicate that structural features related to $\langle n \rangle$ are robust for a given drying protocol, varying little with initial configuration or with different realizations of thermal noise.

Accompanying these trends in coordination are changes in the number M_{void} (within a fixed area) and size of voids outlined by interconnecting strips of nanoparticles. Computationally, we identify voids in a particular configuration with the aid of a superimposed lattice. Specifically, we divide the simulation box into square lattice cells, each with side length l. A cell is designated as occupied if it overlaps any portion of any nanoparticle; otherwise, it is considered unoccupied. Voids then comprise connected clusters of unoccupied lattice cells. A void's size a_{void} is defined as the number of cells belonging to the cluster multiplied by the cell area l^2. The results plotted in Figure 6b,c were obtained with a resolution $l = 0.25D_c$, i.e., with a 140×140 lattice superimposed on configurations of area $35D_c \times 35D_c$. They are reasonably insensitive to the choice of lattice resolution, provided l is small compared to individual particles yet large compared to typical spacing between adjacent particles. Our calculations yield consistent results for values of l between $0.25D_c$ and $1.2D_c$.

The statistics of void density $\rho_{\text{void}} = M_{\text{void}}/L^2$ and geometry depend non-monotonically on quench depth like those of coordination, though in a somewhat less robust way. As shown in Figure 6b,c, the average number of voids per unit area $\langle \rho_{\text{void}} \rangle$ is minimum and the average void size $\langle a_{\text{void}} \rangle$ is maximum at $A' = 2.25$, as foreshadowed by trends in $\langle n \rangle$. Unlike our coordination results, void sizes at a given set of drying conditions can deviate substantially from the mean. In particular, for $A' = 2.25$ and 3, we find 1 in 10 assembled structures that exhibit exceptionally large voids. In both cases these outliers arise from initial configurations with lower-than-average particle densities. Given that stripe thicknesses are narrowly distributed at each value of A', it seems reasonable that low-density initial conditions can yield atypically large voids. Note, however, that assembly trajectories repeated from these same initial conditions, differing algorithmically only in seed values used to initiate generation of random numbers,

produced voids much closer in size to their respective averages. While low initial densities appear to raise the possibility for extremely large voids, this fate is not inevitable. Such large fluctuations in global network structure imply a significant susceptibility to appropriate external forces that warrants further exploration in simulations and might be exploited in the laboratory.

Mechanisms through which the faceted cellular structures of Figure 4b−f arise dynamically from looser and more uniform networks like those of Figures 3b and 4a involve the rupture of thin dipolar chains as an essential component. This process advances rearrangements that favorably lower the energy associated with short-ranged, isotropic attractions: A chain of particles connecting two nodes of a network can, once ruptured, collapse to form numerous contacts with particles near the nodes or with other intact chains. But strong dispersion forces can also contribute to free energy barriers that hinder this basic event. The trends we have discussed in coordination and void statistics can be understood in terms of this fundamental competition between stability and kinetic accessibility, since the severing of chains promotes both enlargement of voids and thickening of their boundaries.

We have explored the influence of strong, short-ranged attractions on the kinetics of chain rupture by simulating the dynamics of isolated chains. We begin with a single-file line of $N_{\text{chain}} = 15$ particles, whose dipoles are arranged head-to-tail, that is rendered infinitely long by connections to its periodic images. Using the same dynamic rules and value of λ as in self-assembly trajectories, we evolve the chain in time for 350 000 MC time steps. This process is repeated 20 times for each value of A' in order to determine a mean first passage time for breakage (τ_{break}).

As an order parameter for chain rupture in these idealized simulations, we monitor the average number of chain neighbors per particle,

$$n^{(\text{chain})} = \frac{1}{N_{\text{chain}}} \sum_{i=1}^{N_{\text{chain}}} \left[H(1.8D_c - r_{i,i+1}) + H(1.8D_c - r_{i,i-1}) \right]$$

$$(7)$$

where the Heaviside step function $H(x) = 1$ for $x \geq 0$ and vanishes otherwise. Indexing of interparticle distances $r_{i,j}$ in Figure 6 refers to the chain's initial state, in which particle i contacts particles $i-1$ and $i+1$ (with the exception of the first and last particles, which contact one another through periodic boundary conditions). For that straight configuration, $n^{(\text{chain})} = 2$. When, in the course of spontaneous fluctuations, $n^{(\text{chain})}$ falls permanently below a threshold of 1.8, we consider the chain to have broken.

As A' increases, the thermodynamic stability of the connected chain clearly decreases relative to that of a compact cluster, which provides several more contacts per particle. The kinetics of chain rupture, however, systematically oppose this trend. Figure 7 shows that the breakage rate declines with increasing A' in a nearly Arrhenius fashion. (Since A sets the scale of dispersion interactions relative to temperature, changing A has the same effect as a proportionate change in $1/T$, neglecting the influence of dipolar interactions on the these dynamics.) Collapse of an anchored chain, while thermodynamically favored, thus requires an activating fluctuation that first raises the energy of short-range attractions.

The behavior of simulated assembly trajectories manifests the implications of these schematic single-chain calculations. For smaller values of A', barriers to chain rupture are low, and

844

dx.doi.org/10.1021/ja107138x |*J. Am. Chem. Soc.* 2011, 133, 838–848
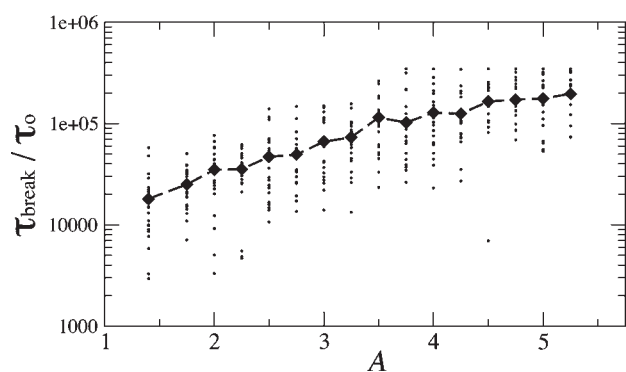
Figure 7. Rupture dynamics for a single chain of 15 aligned particles, whose first and last units are connected through periodic boundaries. The number of MC sweeps preceding spontaneous breakage, τ_{break}/τ_0, is plotted as a function of short-range attraction strength A, where τ_0 represents the time corresponding to one MC sweep. Small points show results for each of 20 individual rupture trajectories at each value of A; larger diamonds show the mean first passage times estimated from these simulations. The dipole strength $\lambda = 6.2$ is identical in all cases. Trajectories in which the chain remained intact following 3.5×10^5 MC sweeps were aborted. These events (not indicated in the plot of τ_{break}) were discarded for the purpose of estimating mean first passage times, which are therefore biased downward. No trajectories required such truncation for $A < 3.75$. The numbers of aborted trajectories for simulations involving stronger short-range attractions were 1 ($A = 3.75$), 3 ($A = 4.5$), 3 ($A = 4.75$), 1 ($A = 5.0$), and 2 ($A = 5.25$).
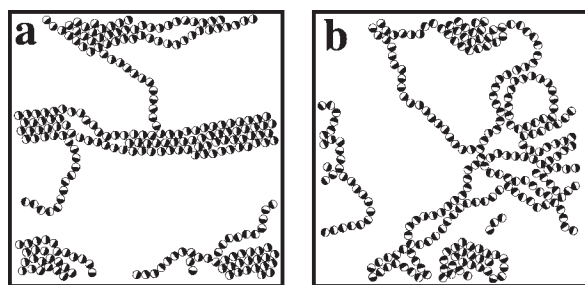
Figure 8. Example products of simulations in which (a) new material was gradually introduced across the initially empty simulation box and (b) trajectories were initiated with all particles placed simultaneously at random. In each case, $A = 1$, $\lambda = 11$, $N = 490$, $L = 35D_c$.

breakdown of intermediate network structures is correspondingly facile. Only the most stable chains, typically those that join with additional parallel chains to form thick strips, survive over long times. In this regime, increasing A' strengthens the tendency for severed chains to remain so and suppresses formation of new network connections. As a result, void sizes increase, and their bounding walls thicken through chain collapse. Overly strong dispersion forces, on the other hand, erect sizable barriers that kinetically stabilize network connections. Here, increasing A' further hampers topological reorganization; void sizes decrease toward values typical of locally equilibrated intermediate configurations, and their boundaries become thinner as routes to chain collapse effectively close.

Spatially Heterogeneous Drying. For sufficiently strong interparticle attractions, aggregation on the substrate could outpace relaxation even at the stage of deposition. Though this regime can be accessed by making λ very large, we find that values realistic for the largest nanocrystals we have synthesized still permit equilibration in the course of straightforward deposition

simulations. In these calculations we add new material, in the form of linear chains comprising between one and seven aligned particles, to fluctuating quasi-2d systems at a fixed rate (200 000 MC sweeps between insertion steps), with positions selected at random. (Addition moves that would result in steric overlap are rejected.)

The example product of this protocol shown in Figure 8a, featuring tightly bundled chains, is qualitatively indistinguishable from equilibrium configurations at the final density. In fact, the gradual deposition of material actually enhances relaxation. Trajectories initiated with all particles placed simultaneously at random, on the other hand, tend to become trapped in states with interconnected networks of chains (Figure 8b).

These results suggest that systems with large but realistic values of λ relax slowly at long wavelengths but can adapt adequately to the perturbations imposed by gradual, spatially uniform deposition. Spatially *heterogeneous* deposition, on the other hand, could introduce density variations that do not decay on observable time scales. Such inhomogeneities can easily arise during evaporation dynamics dominated by nucleation and growth of vapor bubbles, as discussed in ref 41. In the remainder of this section, we describe our attempt to mimic nonuniform deposition and its dramatic impact on the self-assembly of magnetic nanoparticles.

An explicit treatment of the solvent density fluctuations that give rise to transient heterogeneities in solute deposition lies beyond the scope of this work. Instead, we explore here a schematic representation of one of their consequences. Motivated by our experimental observations of large, well-isolated aggregates, we consider a deposition process that is mesoscopically localized. As in the deposition simulations described above, we add material at a fixed rate (200 000 or 500 000 MC sweeps between insertion steps) relative to particles' motion on the substrate, rejecting changes that would violate steric constraints. But in this case particles are introduced only within a limited area, more specifically $10 \pm 3D_c$ from the center of mass of the existing assembly structure. Periodic boundary conditions and correspondingly Ewald summation for long-range interactions are not employed in these calculations. As in the simulations illustrated by Figure 8a, we add particles not individually but in clusters, as appropriate for the strong dipolar interactions under consideration. For the values of λ we use here, even dilute nanoparticles would be present in the overlying solution, predominantly in the form of rings and chains. The qualitative nature of our heterogeneous drying results does not change when particles are added one at a time, since they rapidly associate on the substrate to form ring- and chain-like structures.

The assembly trajectories we propagate in this way differ in essential ways from those described thus far. Most importantly, they proceed in a hierarchical fashion. Dipolar chains, either directly introduced or spontaneously formed on the substrate, are bound with sufficient strength that they maintain integrity over long times. In effect, they serve as the agents of assembly at larger scales.

Effective interactions among these chain "molecules" can be surprisingly complicated. Even for perfectly straight chains, potentials of mean force can be simply anticipated from the form of u_{ij} only when scales of separation r and/or chain length d greatly exceed the size D_c of individual nanoparticles. For $r \gg d \gg D_c$, chains appear to one another as renormalized point dipoles, which attract or repel, depending on orientation, just as in eq 1. In a different extreme limit, when $d \gg r \gg D_c$, the

845

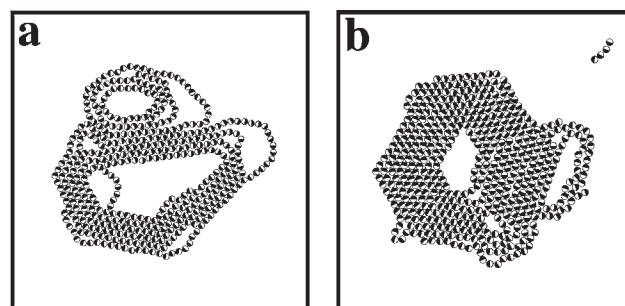dx.doi.org/10.1021/ja107138x |*J. Am. Chem. Soc.* 2011, 133, 838–848
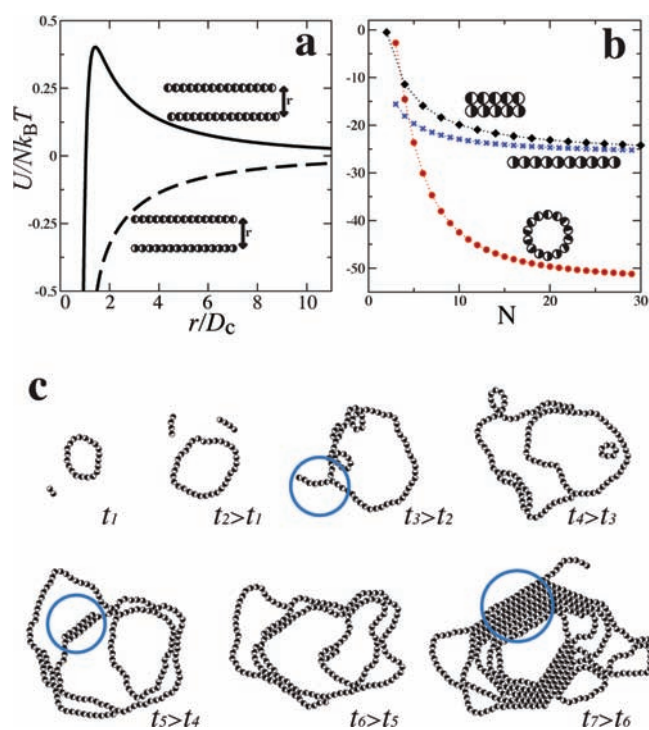
Figure 9. Association of chains of strongly dipolar particles (with $A = 0$ and $\lambda = 19$) in the course of spatially heterogeneous drying simulations. (a) Potential energy U per particle of configurations in which two straight chains (each comprising 15 aligned particles) are separated by a distance r. In the case of antiparallel interchain alignment, chains are positioned horizontally in register (where vertical refers to the direction of separation), as is most energetically favorable. Parallel chains are instead shifted one-half particle diameter out of register, allowing for very favorable interactions at small separations. (b) Potential energy per particle for configurations of N particles arranged as two contacting antiparallel chains (in horizontal register), as a single straight chain, and as a circular ring. (c) Time sequence of an assembly trajectory producing a large angular loop motif. In the course of this MC simulation, small chains are gradually added to a finite area, mimicking heterogeneous deposition from an evaporating solution.

Figure 10. Example products of spatially heterogeneous drying simulations, in which small rings and chains of particles are introduced gradually and locally. (a) Only steric and dipolar interactions have been included ($A = 0$, $\lambda = 19$). (b) Simulation also includes weak, short-range attractions ($A = 1$, $\lambda = 11$).

interchain force per particle is extremely weak; an infinite and continuous line of dipole density in fact exerts no electric field on its surroundings at all.

For two chains of modest length, these limits assist only in understanding the very initial steps of approach. Once D_c is comparable to the separation distance r, the intrinsic granularity of such aggregates becomes an essential and nontrivial consideration. As an example, we show in Figure 9a as a function of r the total potential energy of interaction between two straight chains of equal length, both oriented perpendicular to the direction of separation. At large separations, these calculations evince the r^{-3} repulsion (attraction) expected for parallel (antiparallel) point dipoles in this geometry. Substantial deviations from that ideal behavior begin already at separations of several particle diameters. Because we have shifted the parallel chains horizontally out of register, very favorable energies can be achieved at small separation, where discrete dipoles of one chain nestle between those of the other chain. As a result, even parallel chains can attract sharply near contact. Once they enter this attractive well, further rearrangement can require surmounting an appreciable energy barrier. Internal fluctuations in chains' conformations, asymmetry in their lengths, rotations relative to one another, and

mediation by forces from additional clusters can render even "bimolecular" association complex.

In addition to binding that leaves chains' identities intact, such encounters may effect "chemical" reactions in which they exchange material or fuse to form a larger chain-like structure. As an example, we compare in Figure 9b the potential energy of two contacting antiparallel chains with the energies of a straight chain and of a circular ring with the same mass, which could be obtained from the antiparallel structure by breaking geometrically appropriate contacts. For chains longer than a few particles, the ring is energetically preferred. Soft modes associated with long-wavelength deformations of the ring's contour should provide an entropic advantage as well.

Figure 9c shows snapshots from an example assembly trajectory, initiated with a single small cluster on the substrate. This seed aggregate, a dipolar ring comprising 19 particles, would not be uncommon in a dilute overlying solution for the interaction parameters studied here. It serves to center the growing assembly and focuses attention on loop topologies like those in Figure 1. Chains added outside the initial loop diffuse translationally and rotationally with a weak bias from interactions with the ring. Typically, one end of these added clusters will meet the loop to form a three-way junction (e.g., the circled feature in the snapshot of time t_3 in Figure 9c) not unlike those of sparse networks previously described in the adiabatic drying cases. In many cases, the new chain then rotates to form additional contacts with the ring in a locally parallel orientation, as exemplified by the arrangement of particles circled at t_5 in Figure 9c. At early times, such binding events are followed by rearrangements that incorporate added material into a single larger ring. Ring growth proceeds by this mechanism until accretion outpaces the kinetics of annealing these junctions, or until fluctuations in ring shape lead to large-scale topological changes.

When new material attaches to the growing loop more quickly than junctions can anneal, interactions among added chains become important. One common consequence of nearby additions along the ring is a layering of locally parallel binding (circled particles in Figure 9c, t_7). The thickening of these layers is nearly irreversible, as relaxation would require the sequential crossing of several high energy barriers. The final snapshot in Figure 9c is representative of the fate of loops whose growth is arrested in this fashion. A large central void marks its intermediate ring-like nature; a smooth exterior reflects the chain-by-chain growth mechanism. Asymmetry in the overall contour (i.e., resemblance to an irregular polygon) arises from softness of ring deformations before the onset of

layering, which effectively freezes in a fluctuation in loop shape. Layering itself stems from the kinetic trap of parallel binding, compounded by reinforcement from interfering chain additions. Similarly layered loop structures form via this mechanism in all 10 trajectories we have generated with the parameter sets described in Figure 10, $(A, \lambda) = (1, 11)$ and $(0, 19)$. For the wider range of parameters we explored, $A = 0, 1$ and $\lambda = 10-19$, loop structures were observed in approximately 85% of the trajectories.

These layered loop structures share many unusual features with some of the most intriguing aggregates we have observed in experiments, specifically those depicted in Figure 1. Significant differences are primarily limited to a lack of local compactness in parts of the loop and, in some cases, overall scale. The former discrepancy can be resolved by inclusion of dispersion forces, which were omitted in the simulations described above in order to focus attention on the role of dipolar interactions (see Figure 10). In consideration of the latter difference, we note that exceptionally large layered loops (Figure 1a) identified in experiments are accompanied by exceptionally long chains in their surroundings. While the nonequilibrium evolution or unusual interactions that generate these extended chains is unclear to us, the mechanism we have outlined for association among shorter chains could certainly apply to their subsequent aggregation.

CONCLUSIONS

Our computer simulations indicate that the long-ranged, anisotropic forces acting between magnetic nanoparticles can generate mechanisms of drying-mediated self-assembly quite distinct from those of non-dipolar particles. Indeed, we have observed in experiments long-lived spatial patterns with unprecedented features, e.g., hollow domains and faceted cellular networks. The latter, percolating morphologies are topologically akin to structures characteristic of non-dipolar assembly in heterogeneously evaporating solution, but they arise in a very different way. Here, network connectivity reflects an intrinsic preference for head-to-tail organization, rather than tracing the fronts of expanding vapor bubbles. The propensity for network formation, and its susceptibility to external fields, should correspondingly differ in important ways.

The effects of magnetism in our model arise from interactions identical in form to those between electric dipoles. We nevertheless expect certain aspects of magnetic nanoparticle assembly to be unique. Common solvents screen electrostatic interactions much more strongly than magnetostatic forces. As a result, the effective forces between electric dipoles would be modulated by the process of desolvation in ways that are negligible for magnetic moments. The quenching dynamics we have discussed in the spatially homogeneous drying case, which generate highly networked patterns, should be particularly sensitive to this change.

The emergence of dipolar rings and chains as bound entities that can associate to form higher-order patterns bears a rough but intriguing resemblance to hierarchical mechanisms of biomolecular self-assembly. From proteins' quaternary structures to large multimeric complexes to the actin cytoskeleton, the organization within living cells suggests that assembly through aggregation of progressively larger bound units can attain both robustness and malleability. The strong-dipole regime of drying-mediated magnetic nanoparticle self-assembly may thus present a valuable opportunity for mimicking an aspect of control in biology that has remained elusive in synthetic systems.

ASSOCIATED CONTENT

S **Supporting Information.** TEM images of self-assembled ε-Co nanoparticles. This material is available free of charge via the Internet at http://pubs.acs.org.

AUTHOR INFORMATION

Corresponding Author
geissler@cchem.berkeley.edu

Present Addresses
§Institute for Critical Technology and Applied Science, 233 ICTAS, Stanger Street, Blacksburg, VA 24061, and Department of Geosciences, Virginia Tech, Blacksburg, VA 24061.

ACKNOWLEDGMENT

REFERENCES

(1) Connolly, J.; St. Pierre, T. G.; Rutnakornpituk, M.; Riffle, J. S. *J. Phys. D: Appl. Phys.* **2004**, *37*, 2475–2482.

(2) Morales, M. P.; Serna, C. J.; Bodker, F.; Morup, S. *J. Phys.: Condens. Matter.* **1997**, *9*, 5461.

(3) Kim, D. K.; Mikhaylova, M.; Wang, F. H.; Kehr, J.; Bjelke, B.; Zhang, Y.; Tsakalakos, T.; Muhammed, M. *Chem. Mater.* **2003**, *15*, 4343–4351.

(4) Sun, M.; Zangari, G.; Shamsuzzoha, M.; Metzger, R. M. *Appl. Phys. Lett.* **2001**, *78*, 2964.

(5) Pileni, M.-P.; Duxin, N. *Chem. Innov.* **2000**, *30*, 25.

(6) Roullin, V.-G.; Deverre, J.-R.; Lemaire, L.; Hindre, F.; Venier-Julienne, M.-C.; Vienet, R.; Benoit, J.-P. *Eur. J. Pharm. Biopharm.* **2002**, *53*, 293–299.

(7) Portet, D.; Denizot, B.; Rump, E.; Lejeune, J. J.; Jallet, P. *J. Colloid Interface Sci.* **2001**, *238*, 37–42.

(8) Sun, S.; Murray, C. B.; Weller, D.; Folks, L.; Moser, A. *Science* **2000**, *287*, 1989–1992.

(9) Chen, M.; Kim, J.; Liu, J. P.; Fan, H.; Sun, S. *J. Am. Chem. Soc.* **2006**, *128*, 7132–7133.

(10) Sun, S. *Adv. Mater.* **2006**, *18*, 393–403.

(11) Moser, A.; Takano, K.; Margulies, D. T.; Albrecht, M.; Sonobe, Y.; Ikeda, Y.; Sun, S.; Fullerton, E. E. *J. Phys. D: Appl. Phys.* **2002**, *35*, R157–R167.

(12) Lazzari, M.; Rodriguez-Abreu, C.; Rivas, J.; Lopez-Quintela, M. A. *J. Nanosci. Nanotechnol.* **2006**, *6*, 892–905.

(13) Ariga, K.; Hill, J. P.; Lee, M. V.; Vinu, A.; Charvet, R.; Acharya, S. *Sci. Technol. Adv. Mater.* **2008**, *9*, 014109.

(14) Alivisatos, A.; Barbara, P.; Castleman, A.; Chang, J.; Dixon, D.; Klein, M.; McLendon, G.; Miller, J.; Ratnet, M.; Rossky, P.; Stupp, S.; Thompson, M. *Adv. Mater.* **1998**, *10*, 1297–1336.

(15) Whitesides, G. M.; Grzybowski, B. *Science* **2002**, *295*, 2418–2421.

(16) Manna, L.; Scher, E. C.; Alivisatos, A. P. *J. Am. Chem. Soc.* **2000**, *122*, 12700–12706.

(17) Perro, A.; Reculusa, S.; Ravaine, S.; Bourgeat-Lami, E.; Duguet, E. *J. Mater. Chem.* **2005**, *15*, 3745–3760.

(18) Maksimuk, S.; Teng, X.; Yang, H. *Phys. Chem. Chem. Phys.* **2006**, *8*, 4660–4663.

(19) Nie, W.; He, J.; Zhao, N.; Ji, X. *Nanotechnology* **2006**, *17*, 1146–1149.

(20) Zettsu, N.; McLellan, J. M.; Wiley, B.; Yin, Y.; Li, Z.-Y.; Xia, Y. *Angew. Chem., Int. Ed.* **2006**, *118*, 1310–1314.

(21) Zhang, Z.; Keys, A. S.; Chen, T.; Glotzer, S. C. *Langmuir* **2005,** *21*, 11547–11551.

(22) Iacovella, C. R.; Glotzer, S. C. *Nano Lett.* **2009,** *9*, 1206–1211.

(23) Zhang, Z.; Horsch, M. A.; Lamm, M. H.; Glotzer, S. C. *Nano Lett.* **2003,** *3*, 1341–1346.

(24) Cheng, L.; Hou, G.; Miao, J.; Chen, D.; Jiang, M.; Zhu, L. *Macromolecules* **2008,** *41*, 8159–8166.

(25) Puntes, V. F.; Krishnan, K. M.; Alivisatos, A. P. *Science* **2001,** *291*, 2115–2117.

(26) Whitelam, S.; Geissler, P. L. *J. Chem. Phys.* **2007,** *127*, 154101.

(27) Whitelam, S.; Feng, E. H.; Hagan, M. F.; Geissler, P. L. *Soft Matter* **2009,** *5*, 1251–1262.

(28) Tang, Z.; Zhang, Z.; Wang, Y.; Glotzer, S. C.; Kotov, N. A. *Science* **2006,** *314*, 274–278.

(29) Hagan, M. F.; Chandler, D. *Biophys. J.* **2006,** *91*, 42–54.

(30) Wilber, A. W.; Doye, J. P. K.; Louis, A. A.; Noya, E. G.; Miller, M. A.; Wong, P. *J. Chem. Phys.* **2007,** *127*, 085106.

(31) Horsch, M. A.; Zhang, Z.; Glotzer, S. C. *Phys. Rev. Lett.* **2005,** *95*, 56105.

(32) Mutch, K. J.; Koutsos, V.; Camp, P. J. *Langmuir* **2006,** *22*, 5611–5616.

(33) Tang, J.; Ge, G.; Brus, L. E. *J. Phys. Chem. B* **2002,** *106*, 5653–5658.

(34) Palmer, J. S.; Swaminathan, P.; Babar, S.; Weaver, J. H. *Phys. Rev. B* **2008,** *77*, 195422.

(35) Cheng, W.; Dong, S.; Wang, E. *J. Phys. Chem. B* **2005,** *109*, 19213–19218.

(36) Vysotskii, V. V.; Roldughin, V. I.; Uryupina, O. Y. *Colloid J.* **2004,** *66*, 777–779.

(37) Kletenik-Edelman, O.; Ploshnik, E.; Salant, A.; Shenhar, R.; Banin, U.; Rabani, E. *J. Phys. Chem. C* **2008,** *112*, 4498–4506.

(38) Martin, C. P.; Blunt, M. O.; Pauliac-Vaujour, E.; Stannard, A.; Moriarty, P.; Vancea, I.; Thiele, U. *Phys. Rev. Lett.* **2007,** *99*, 116103/1–116103/4.

(39) Martin, C. P.; Blunt, M. O.; Moriarty, P. *Nano Lett.* **2004,** *4*, 2389–2392.

(40) Stannard, A.; Martin, C. P.; Pauliac-Vaujour, E.; Moriarty, P.; Thiele, U. *J. Phys. Chem. C* **2008,** *112*, 15195–15203.

(41) Rabani, E.; Reichman, D. R.; Geissler, P. L.; Brus, L. E. *Nature* **2003,** *426*, 271–274.

(42) Ge, G.; Brus, L. *J. Phys. Chem. B* **2000,** *104*, 9573–9575.

(43) Bray, A. J. *Adv. Phys.* **1994,** *43*, 357–459.

(44) Blunt, M. O.; Martin, C. P.; Ahola-Tuomi, M.; Pauliac-Vaujour, E.; Sharp, P.; Nativo, P.; Brust, M.; Moriarty, P. J. *Nat. Nanotechnol.* **2007,** *2*, 167–170.

(45) Vancea, I.; Thiele, U.; Pauliac-Vaujour, E.; Stannard, A.; Martin, C. P.; Blunt, M. O.; Moriarty, P. J. *Phys. Rev. E* **2008,** *78*, 041601.

(46) Pauliac-Vaujour, E.; Stannard, A.; Martin, C. P.; Blunt, M. O.; Notingher, I.; Moriarty, P. J.; Vancea, I.; Thiele, U. *Phys. Rev. Lett.* **2008,** *100*, 176102.

(47) Moriarty, P.; Taylor, M. D. R.; Brust, M. *Phys. Rev. Lett.* **2002,** *89*, 248303.

(48) Dinega, D. P.; Bawendi, M. G. *Angew. Chem., Int. Ed.* **1999,** *38*, 1788–1791.

(49) Bao, Y.; Beerman, M.; Krishnan, K. M. *J. Magn. Magn. Mater.* **2003,** *266*, L245–L249.

(50) Song, Q.; Ding, Y.; Wang, Z. L.; Zhang, Z. J. *J. Phys. Chem. B* **2006,** *110*, 25547–25550.

(51) Wang, Z. L.; Dai, Z.; Sun, S. *Adv. Mater.* **2001,** *12*, 1944–1946.

(52) Lalatonne, Y.; Richardi, J.; Pileni, M. P. *Nat. Mater.* **2004,** *3*, 121–125.

(53) Morimoto, H.; Maekawa, T. *Int. J. Mod. Phys. B* **1999,** *13*, 2085–2092.

(54) Weis, J. J. *J. Phys.:Condens. Matter* **2003,** *15*, S1471–S1495.

(55) Gao, G. T.; Zeng, X. C.; Wang, W. *J. Chem. Phys.* **1997,** *106*, 3311–3317.

(56) Tay, K.; Bresme, F. *Mol. Simul.* **2005,** *31*, 515–526.

(57) Patel, N.; Egorov, S. A. *J. Chem. Phys.* **2007,** *126*, 054706.

(58) Schapotschnikow, P.; Pool, R.; Vlugt, T. J. H. *Nano Lett.* **2008,** *8*, 2930–2934.

(59) Israelachvili, J. *Intermolecular and Surface Forces*, 2nd ed.; Academic Press: San Diego, CA, 2003.

(60) Hamaker, H. C. *Physica* **1937,** *4*, 1058–1072.

(61) Frenkel, D.; Smit, B. *Understanding Molecular Simulation: from Algorithms to Applications*, 2nd ed.; Academic Press: San Diego, CA, 2002.

(62) Allen, M. P.; Tildesley, D. J. *Computer Simulation of Liquids*; Oxford University Press: New York, 1989.

(63) Yosef, G.; Rabani, E. *J. Phys. Chem. B* **2006,** *110*, 20965–20972.

(64) Held, G. A.; Grinstein, G.; Doyle, H.; Sun, S.; Murray, C. B. *Phys. Rev. B* **2001,** *64*, 012408.

(65) Butter, K.; Bomans, P. H. H.; Frederik, P. M.; Vroege, G. J.; Philipse, A. P. *Nat. Mater.* **2003,** *2*, 88–91.

(66) Duncan, P. D.; Camp, P. J. *J. Chem. Phys.* **2004,** *121*, 11322–11331.

(67) Weis, J. J.; Tavares, J. M.; Telo da Gama, M. M. *J. Phys.: Condens. Matter.* **2002,** *14*, 9171–9186.

(68) Stevens, M. J.; Grest, G. S. *Phys. Rev. E* **1995,** *51*, 5962–5975.

(69) Weis, J. J.; Levesque, D. *Phys. Rev. Lett.* **1993,** *71*, 2729–2732.

(70) Zubarev, A. Y.; Iskakova, L. Y. *Phys. Rev. E* **2007,** *76*, 061405.

(71) Kim, B.; Carignano, M. A.; Tripp, S. L.; Wei, A. *Langmuir* **2004,** *20*, 9360–9365.

(72) Kim, B.; Tripp, S. L.; Wei, A. *J. Am. Chem. Soc.* **2001,** *123*, 7955–7956.